e-ISSN: 2550-164X

Available online at
https://jmeche.uitm.edu.my/

Journal of Mechanical Engineering 23(2) 2026, 118 – 134.

Journal of Mechanical Engineering

Design and Performance Optimization of a Layered Rotational Polymer–Metal Triboelectric Nanogenerator as an Enhanced Energy Harvester

Muhammad Irsyad Missnan[1], Oskar Hasdinor Hassan [2,3*], Muhammad Aman Haikal Razali[2], Mohd Amirul Ramlan[4,5], Ainnur Sherene Kamisan[1], Panu Thainiramit[6], Nur Hamizah Mohd Zaki[1,2], Ahmad Sukri Ahmad[7], Tunku Ishak Tunku Kudin[7,8], Mohamad Fariz Mohamad Taib[1]

[1]*Faculty of Applied Sciences, Universiti Teknologi MARA, 40450 Shah Alam, Selangor, Malaysia*
[2]*Ionic Materials and Devices (iMADE), Institute of Science, Universiti Teknologi MARA, 40450 Shah Alam, Selangor, Malaysia*
[3]*College of Creative Arts, Universiti Teknologi MARA, 40450 Shah Alam, Selangor, Malaysia*
[4]*Faculty of Mechanical Engineering, Universiti Teknologi MARA, 40450 Shah Alam, Selangor, Malaysia*
[5]*Jabatan Pendidikan Politeknik dan Kolej Komuniti, Ministry of Higher Education, Malaysia*
[6]*Division of Physical Science (Physics), Faculty of Science, Prince of Songkla University, Songkhla, Thailand*
[7]*Renewable Technology Program PETRONAS Group Research & Technology, 43000 Bandar Baru Bangi, Selangor, Malaysia*
[8]*Faculty of Defence Science and Technology, Universiti Pertahanan Nasional Malaysia (UPNM)*

ARTICLE INFO

Article history:
Received 13 October 2025
Revised 18 February 2026
Accepted 07 April 2026
Online first
Published 15 May 2026

Keywords:
Triboelectric nanogenerator
Copper
PTFE
Polymer-metal TENG

DOI:
10.24191/jmeche.v23i2.9195

ABSTRACT

The need for sustainable energy solutions has driven research into energy harvesting technologies, and triboelectric nanogenerators (TENGs) offer an effective means of converting mechanical energy into electricity. This study presents a novel friction-based rotating triboelectric nanogenerator (FR-TENG) that employs a layered polymer-metal configuration in a sliding, freestanding mode. The apparatus comprises five vertically aligned FR-TENG units connected in parallel, thereby improving electrical output. The single-unit FR-TENG generates a peak open-circuit voltage (V_{oc}) of 116-131 V and a short-circuit current (I_{sc}) of 7.4-10.5 µA at 200 rpm. The stacked configuration significantly enhances performance, yielding a 145% increase in V_{oc} output and up to a 240% rise in current output, achieving a maximum of 285 V and 27.6 µA at 200 rpm. The optimized combination of polytetrafluoroethylene (PTFE) and copper enhances charge-transfer efficiency, with segmentation and surface-area modifications further improving performance. The generated energy suffices to power LEDs, demonstrating the viability of self-sustaining electronic applications. This study presents a systematic approach to improve TENG efficiency by optimizing material selection and device design, thereby facilitating scalable energy-harvesting solutions for IoT and low-power electronic applications.

[3*] Corresponding author. *E-mail address*: oskar@uitm.edu.my
https://doi.org/10.24191/jmeche.v23i2.9195

INTRODUCTION

In the past decade, the growth of renewable energy, particularly in energy-harvesting technologies, has accelerated significantly as the demand for sustainable, self-sufficient devices enabled by the Internet of Things (IoT) has risen. Hence, this became the catalyst for the creation of a new energy harvester, the nanogenerator, by Wang & Song (2006). This technology is designed to scavenge ambient mechanical energy that is commonly dissipated through friction, vibration, and rotational mechanical losses in natural and engineered systems (Kim et al., 2021; Yang et al., 2012). Among the ambient mechanical energy available in the surrounding environment are vibrations and frictions, which have always been avoided (Suo et al., 2016).

Frictional mechanical motion was widely recognised as one of the most common sources of dissipated mechanical energy in both natural and industrial environments. In practical mechanical systems, such as rotating machinery (Xin et al., 2022), vehicular components (Zhou et al., 2021), wind-driven structures (He et al., 2021), and fluid flow systems (Wang et al., 2017), a substantial portion of mechanical work is inevitably lost through frictional interactions between contacting surfaces and is typically dissipated as thermal energy (Zhang et al., 2023). Triboelectric nanogenerators (TENGs) developed by Zhong et al (2022) recover this wasted mechanical energy by converting friction-induced contact electrification into usable electrical energy through triboelectrification, which couples electrostatic induction and contact electrification (Han et al., 2014; Fan et al., 2012; Peng et al., 2022). Sliding and rotational friction have been experimentally demonstrated to provide stable, continuous, periodic excitation, making them highly suitable for triboelectric energy harvesting (Chatbouri et al., 2025). Therefore, the rotational friction employed in this study represents a controlled laboratory simulation of the mechanical energy sources commonly found in environmental and industrial systems. The use of motor-driven excitation provides a reproducible approach to characterize electromechanical conversion behavior prior to real-world deployment.

Furthermore, it generates continuous friction, enabling a high, continuous electrical output, making rotation a favourable mechanism for integration into TENG technology (Han et al., 2022). TENG is known to produce an alternating pulse output with high voltage and low current (Bai et al., 2022; Yang et al., 2023). Therefore, proper harvesting methods and power management are necessary to ensure that the low power output of TENG devices is complemented by a continuous, reliable source, thereby providing a steady supply of electricity (Munirathinam et al., 2022; Naval et al., 2023).

In TENG, a wide range of materials can be used as tribo-materials, including polymers and metals (Xin et al., 2022), conductors and insulators (Lin et al., 2013), and solids and gases (Wang et al., 2024). Triboelectrification occurs through friction or contact between two materials with different electron affinities (Fang et al., 2021). Polymer-metal TENG is a key area of focus for improving TENG performance, as it reduces the number of components by using metal as both an electrode and a tribo-positive material. The most well-known pair of polymer-metal materials is polytetrafluoroethylene (PTFE), which is tribo-negative, and copper, which is tribo-positive (Wang et al., 2021; Zhao et al., 2022).

This study focuses on fabricating a friction-based TENG that utilizes rotational motion, integrating triboelectric material optimization, dielectric segmentation, and a multilayer rotational design into a unified system that experimentally validates the theoretical coupling between segmentation-induced charge localization and electrodynamic V-Q-x modelling. This study therefore provides a quantitative geometrical optimization pathway for enhancing polymer–metal TENG performance beyond conventional device stacking strategies, thereby increasing the device's electrical output. The electrical output of the single unit FR-TENG ranges from 116 V to 131 V for the maximum open-circuit voltage (V_{oc}) and short-circuit current (I_{sc}) that range from 7.4 to 10.5 μA. The electrical signal output shows a 50%–60% increase due to the stacked arrangement of five (5) single FR-TENG units with parallel electrical connections between them.

https://doi.org/10.24191/jmeche.v23i2.9195

METHODOLOGY

Working principle

The device employs a sliding freestanding mode, where triboelectrification is triggered by sliding a PTFE over two copper electrodes. This sliding motion generates friction, producing electricity through the coupling of electrostatic induction and contact-separation (Ren et al., 2022; Zhou et al., 2020). PTFE is the tribo-negative material since it has a higher electron affinity compared to copper, based on the fluorine atoms that contribute to the electronegativity of the structure. The counter material is copper, a tribo-positive material that tends to lose electrons due to its metallic conductivity, resulting in free electrons and a lower electron affinity than PTFE (Zou et al., 2020). The works principle of the material used in the device is shown in Fig. 1.

In Fig. 1(a), PTFE is in direct contact with the top left side of the copper (LC). During this state, contact electrification (CE) occurs due to differences in electron affinity. The electron from copper will be transferred to PTFE due to its high electron affinity, leaving PTFE negatively charged. When PTFE starts to slide to the right side of the copper (RC), the electron that is transferred to PTFE remains on the surface due to electrostatic forces induced from the CE, as in Fig. 1(b). The LC will back into the neutral state due to the separation of the PTFE. Fig. 1(c) illustrates the electrostatic induction that the PTFE induces. Hence, a potential difference is created between the two copper wires. It induced the potential difference between them, allowing the electrons to flow through an external circuit to equalize the imbalance in charge. The charges will be redistributed during the PTFE slide back to the initial copper electrodes, diminishing the potential difference as shown in Fig. 1(d). The electron will flow back to its original copper to restore equilibrium. Hence, the current will pulsate back and forth, producing an alternating current (AC).

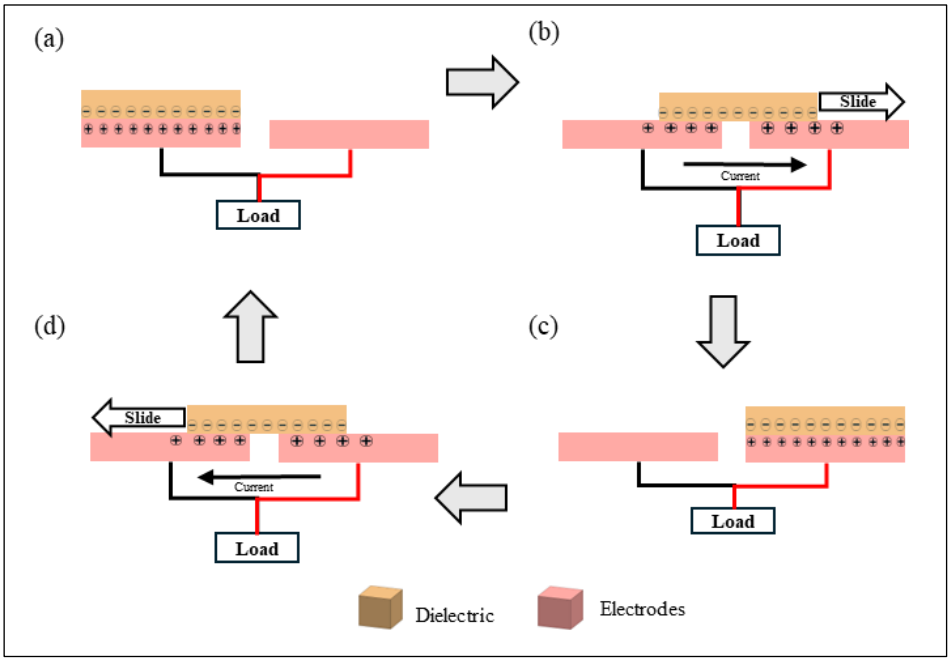

Fig. 1. Illustration of the working principle of the rotational TENG.

https://doi.org/10.24191/jmeche.v23i2.9195

Structural design of the energy harvester

The device consists of five (5) stacked individual FR-TENG units connected in parallel, as shown in Fig. 2(a). The device is 34 cm in diameter and 70.5 cm in height. The multi-layered configuration is the individual unit of the FR-TENG, which contains the friction layer built from the rotor and stator, as shown in Fig. 2(b). Fig. 2(c) shows the substrate for the PTFE (in light brown) named rotor, and Fig. 2(d) shows the stator, the substrate for the copper plate (in reddish-brown). This friction layer or generating components are made up of four (4) radial trapezoidal segments of copper pairs and four (4) PTFE in the exact shape as radial trapezoidal segments. The copper has a total area of 47.59 cm^2, with the inner arc length of 1.64 cm, outer arc length of 8.03 cm, and the radial height of 10 cm for each copper plate. The PTFE has the same radial height, with an inner arc length of 1.31 cm and an outer arc length of 6.54 cm. The total area of a PTFE segment is 39.27 cm^2. All dimensions for the stator, rotor, and device were presented in Table 1. The stator was secured in a location that facilitates all wire connections between the electrodes, thereby enabling the freestanding TENG mode. The rotor was rotated on top of the stator to generate friction that triggers triboelectrification.

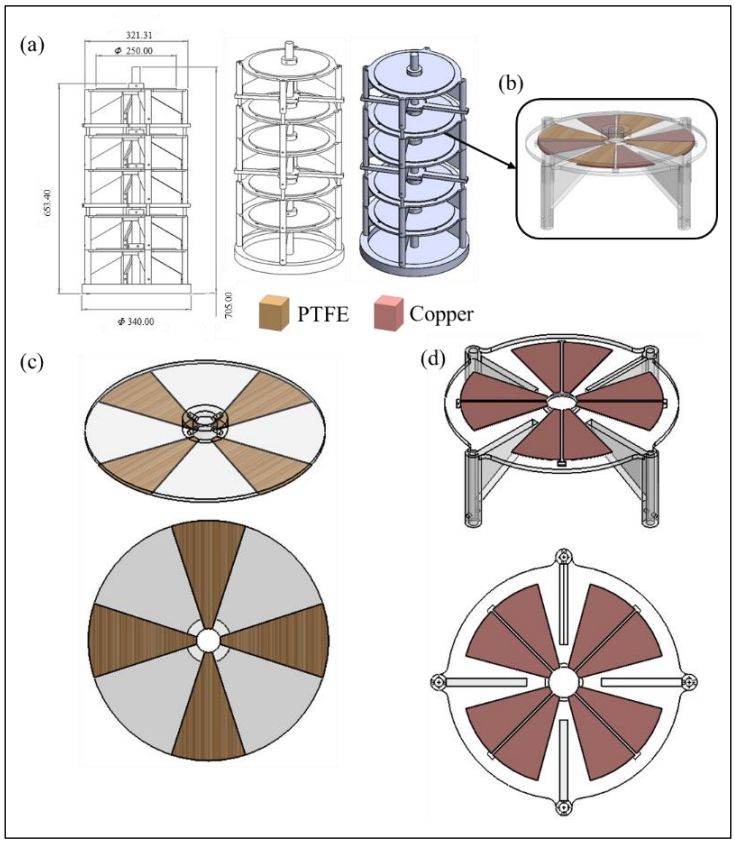

Fig. 2. (a) The stacked FR-TENG device's design, (b) the individual unit of FR-TENG, (c) rotor, the rotation part in the FR-TENG and (d) the stator, the static part in the FR-TENG.

Material preparation and assembly

The materials used were copper (as the tribo-positive material and electrode) and PTFE (as the tribo-negative material). The copper used is a 0.1 mm-thick pure copper plate, and the PTFE is a coated glass

https://doi.org/10.24191/jmeche.v23i2.9195

fabric adhesive tape with a thickness of 0.13 mm. The copper plate was texturized with sandpaper to increase friction between the PTFE and copper, thereby enhancing TE, as shown in Fig. 3(a). Fig. 3(b) shows the pre-texturized copper plate, and Fig. 3(c) shows the texturized copper plate. The texturized copper plates were placed on top of the static acrylic stator substrate, as shown in Fig. 3(d). PTFE tapes were placed on top of the rotating acrylic substrate, or rotor, as shown in Fig. 3(e). The rotor and stator were stacked as shown in Fig. 2(a) prior to performance testing.

Table 1. Dimensions of the rotor, stator, and the devices

Surface area of a single PTFE tape	39.24 cm^2
Surface area of a single copper plate	48.37 cm^2
Thickness of PTFE tape	0.13 mm
Thickness of copper plate	0.10 mm
Number of FR-TENG	5
Total height of stacked FR-TENG	70.50 cm
Diameter of rotor	Φ = 25.00 cm
Diameter of stator	Φ = 29.00 cm

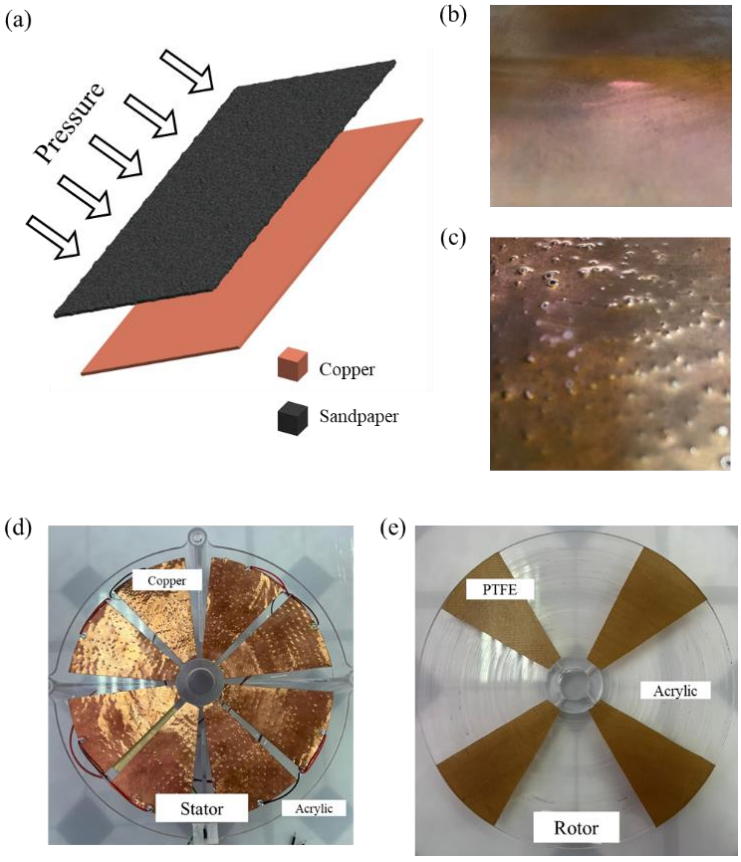

Fig. 3. (a) The texturized process of the copper plate, (b) the smooth copper plate, (c) the texturized copper plate, (d) the copper plate arrangement on top of the stator, and (e) the PTFE tape arrangement on top of the rotor.

https://doi.org/10.24191/jmeche.v23i2.9195

Electrical performance evaluation setup

The performance of the FR-TENG and the Stacked FR-TENG was investigated based on the electrical output (voltage and current) generated by frictional harvesting. Friction was generated by rotation initiated by a controllable electric motor, and the electric power generated was measured using the instruments shown in Fig. 4(a). The electric motor employed in this study serves as a controlled mechanical excitation source to establish reproducible rotational frequencies for characterizing triboelectric output behavior. The use of motor-driven excitation is a standard laboratory methodology that enables precise control of rotational speed, ensuring reliable evaluation of the relationship between mechanical input frequency and electrical output performance.

An electric motor, MY1018-1 24V, was used to initiate friction, and to measure the rotation per minute (RPM), a TENMARS TM4100 Digital Tachometer was used. The RPMs varied from 10 to 200 to measure the device's electrical output. The alternating voltage pulse generated by the device was measured using a Keysight InfiniiVision DSOX3014T Digital Storage Oscilloscope, as shown in Fig. 4(a), and the current was measured using a Kyoritsu Model 1009 multimeter, as shown in Fig. 4(b). A PCB was used to convert the rectified output as shown in Fig. 4(b). The wire was soldered to the copper plate to harvest the charges generated, as shown in Fig. 4(c). Fig. 4(d) shows the parallel connection of each plate to the measuring device.

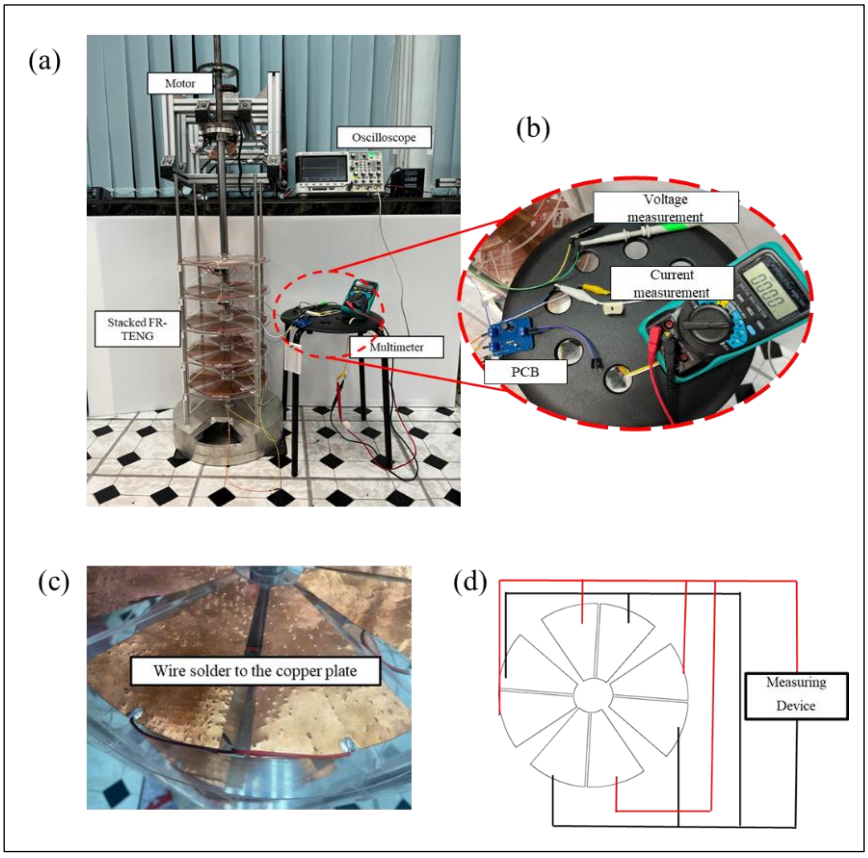

Fig. 4. (a) The whole setup to evaluate the electrical performance of the FR-TENG, (b) the connection of FR-TENG to the measuring device, and (c) the parallel wire connection between the copper plate.

https://doi.org/10.24191/jmeche.v23i2.9195

RESULTS AND DISCUSSION

Dielectric optimization analysis

Previous research has shown that alterations to dielectrics affect the electrical performance of tribo-electrification (Chen et al., 2016; Li et al., 2021). Surface area plays a significant role in triboelectrification, as a large surface area increases electron transfer between the two materials when they come into contact (Gomes et al., 2018; Rana et al., 2022). Other than that, the gap and the number of the dielectric will increase the triboelectric effect. Increasing the number of dielectrics increases the contact surface area, thereby facilitating electron transfer (Shrestha et al., 2023).

Furthermore, the dielectric gap will affect the triboelectric effect through the material's relaxation time, as in a parallel-plate capacitor (CA) (Shao et al., 2020). Hence, two parameters were investigated to increase the device's voltage output: the surface area and the number of dielectric segmentations on the rotating (rotor) substrate. Both results from the investigated parameters were presented in Fig. 5.

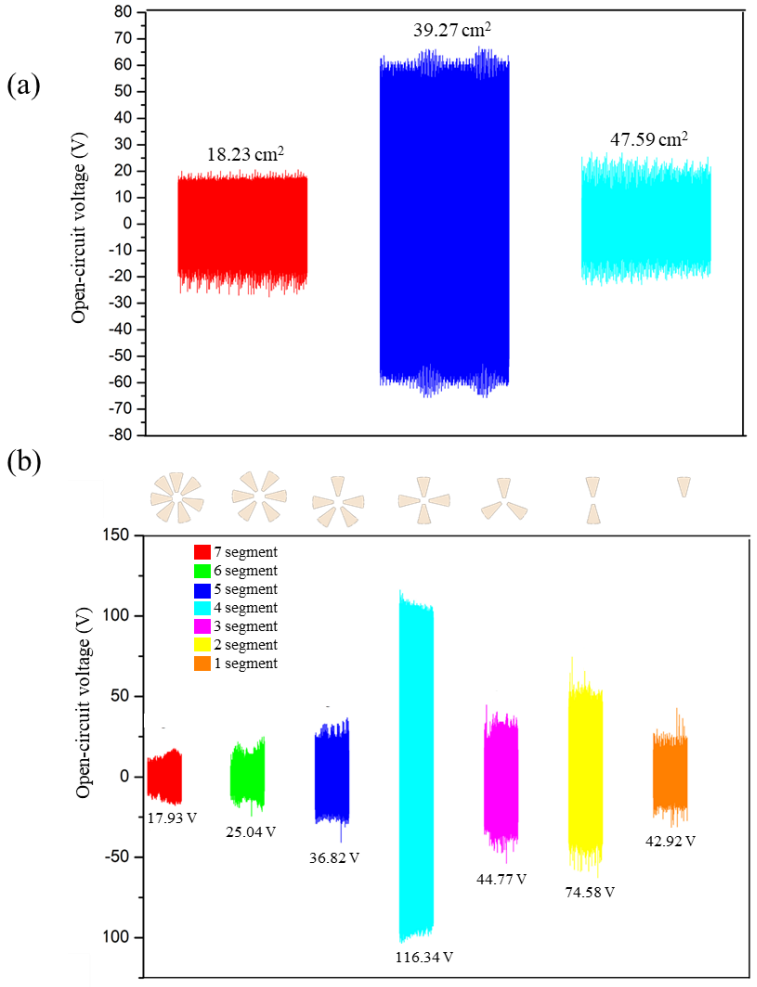

Fig. 5. Analysis on the dielectric optimization affected by (a) the surface area effect on the open-circuit voltage produced at 100 rpm and (b) the influence of the number of PTFE segments on the rotor at 200 rpm.

https://doi.org/10.24191/jmeche.v23i2.9195

Fig. 5(a) shows the effect of the dielectric surface area on the electrical performance of the device. The dielectric tapes were prepared in segmented shapes with three surfaces: 18.23 cm^2, 39.27 cm^2, and 47.59 cm^2, arranged on a 25 cm-diameter rotating substrate. As shown in Fig. 5(a), the voltage output is much higher as the contact surface area of the dielectric increases. Triboelectric interaction largely depends on the amount of charge, Q, that is accumulated on the surface of the material that undergoes the interaction. Hence, the areas of 39.27 cm^2 and 47.59 cm^2 achieved higher maximum values than the 18.23 cm^2 due to the wider contact area, which facilitated charge transfer (Gomes et al., 2018; Xu et al., 2018). A larger dielectric surface area enhances charge accumulation, confirming experimental results and thereby increasing voltage output (Fan et al., 2012). The findings indicate a clear correlation between contact area and triboelectric potential (Liu et al., 2026). The output voltage increases significantly as the area expands, from 18.23 cm^2 to 39.27 cm^2, then to 47.59 cm^2. However, the total area of 47.59 cm^2 showed a significant voltage drop when compared to 39.27 cm^2. Other than an increase of area to improve the triboelectric performance, the charge density, σ determines most of the output since the increase of the area, A, will reduce the charge density (Wang & Wang, 2019), as shown in Equation 1.

$$\frac{Q}{A} = \sigma \tag{1}$$

Moreover, whilst total charge may increase, charge density decreases as it disperses across a larger contact surface area (S), thereby increasing the electrostatic potential difference (Han et al., 2019). Furthermore, contact-mode TENG derived a V-Q-x relationship based on electrodynamics to interpret the interdependence among voltage (V), charge (Q), and displacement ($x(t)$) in transducing frictional force into electrical energy (Niu & Wang, 2015). The relationship defines the fundamental operation and output characteristics of TENG, including the adequate thickness of the material (d_0). Understanding the relationship will increase the output produced by TENG. Equation 2 shows the V-Q-x relationship.

$$V = -\frac{Q}{S\varepsilon_0}(d_0 + x(t)) + V_{oc} \tag{2}$$

In the above equation ε_0 shows as the vacuum permittivity and the open-circuit voltage were denoted as V_{oc} and expressed as Equation 3. This equation defines the open-circuit voltage V_{oc} as directly proportional to the product of surface charge density σ and the instantaneous separation distance $x(t)$, and inversely proportional to the vacuum permittivity ε_0. Equation (4) rearrange the open-circuit voltage in terms of total transferred charge Q and effective contact area A.

$$V_{oc} = \frac{\sigma x(t)}{\varepsilon_0} \tag{3}$$

By relating the surface charge density equation in Equation 1 and the V_{oc} equation, Equation 4 was derived to explain the surface area relationship to the V_{oc} output produced by TENG:

$$V_{oc} = \frac{Q\, x(t)}{A\varepsilon_0} \tag{4}$$

This equation highlights the inverse dependence of voltage on surface area for a given total charge. Specifically, as the contact area increases, the charge is distributed over a larger surface, reducing the

https://doi.org/10.24191/jmeche.v23i2.9195

surface charge density and consequently lowering the electric field strength and output voltage. Conversely, reducing the effective contact area increases charge localization, enhancing the electrostatic potential. This explains the observed dependence of TENG output on dielectric segmentation and justifies the existence of an optimal surface area that balances charge generation and charge density concentration. Hence, an optimal surface area needs to be well-defined to optimize the output, as this study exhibits an optimal dielectric area of 39.27 cm^2.

In Fig. 5(b), the effect of varying the number of electric segments is shown, with the same area of 39.27 cm^2 at a constant 200 rpm for all variations. The dielectric segmentation is arranged from one (1) segment up to seven (7) segments. Variations in the number of segments significantly affected the V_{oc} of TENG. The seven segments of dielectric produced yielded 17.93 V of V_{oc}, which increased to 116.34 V when the number of dielectric segments was reduced to four. Then the V_{oc} decreased as the number of dielectric segments decreased from four to three, then two, and finally one. Four segments (V_{oc} = 116.34 V) exhibit the highest voltage output, indicating the best segmentation arrangement, maximising charge separation and recombination efficiency.

The fundamental mechanism underlying segmentation effects is the improvement of charge localisation and redistribution. Enhancing segmentation improves triboelectric performance by enabling better charge transfer. Reduced segments facilitate more localized contact electrification, leading to a higher charge density (Zou et al., 2020). Nonetheless, exceeding an ideal segmentation threshold leads to over-segmentation, which diminishes the effective contact area for each segment and consequently decreases the voltage output (Wang, 2014).

The findings indicate that triboelectrification in dielectric materials is significantly affected by surface area and segmentation. Although a larger surface area improves charge transfer and voltage generation, an ideal segmentation number exists that best maximizes the triboelectric effect. Future research should investigate how segmentation design and material properties interact to maximise TENG performance for energy-harvesting applications.

Single-unit FR-TENG performance analysis

Fig. 6 shows the electrical performance (V_{oc}, open-circuit voltage, and I_{sc}, short-circuit current) for different rotations of the single-unit FR-TENG using the same material (Cu as the electrode and PTFE as the dielectric). The area of the dielectric was constant with 39.27 cm^2, and the number of dielectric segments was four. Five (5) RTENG units were tested and will be assembled in a stacked, parallel-connection arrangement. Fig. 6(a) presents the sinusoidal V_{oc} produced by a single FR-TENG unit at different rotational speeds from low to high (10 rpm to 200 rpm). The voltage waveforms display clear sinusoidal characteristics, with higher frequency and amplitude correlating with increased rotational speed. At 10 rpm, the FR-TENG produces a maximum V_{oc} of 8 V, increasing to 64 V and 116 V at 100 rpm and 200 rpm, respectively. The increase in V_{oc} produced by the device, resulting from increased rotation speed, indicates an increase in charge transfer due to triboelectrification (Hao et al., 2023).

The same test was conducted on four additional FR-TENG units, denoted 1-5. The V_{oc} produced by each unit was measured, and the resulting sinusoidal waveform is illustrated in Fig. 6(b). The figure shows the output at a constant rotational speed of 100 rpm to compare the difference between each unit. All units exhibit a nearly identical V_{oc}, with voltage waveforms of almost identical frequency and magnitude, ranging from 56 V to 66 V. The percentage difference between the outputs was less than 18%. The homogeneity of the voltage response emphasizes the stability and repeatability of the FR-TENG construction.

Fig. 6(c) shows the measured I_{sc} for each FR-TENG unit (1-5) at rotational speeds from 10 to 200 rpm. I_{sc} exhibited a direct linear relationship with increasing rotation speed. The maximum I_{sc} of each unit was 0.1 μA to 0.4 μA at 10 rpm, increasing to 8.1 μA to 10.5 μA at 200 rpm. This indicates that enhanced mechanical motion boosts charge generation until saturation effects set in (Segkos & Tsamis, 2023; Zhang

https://doi.org/10.24191/jmeche.v23i2.9195

et al., 2023). The same pattern was observed in the measured V_{oc} for each TENG unit; it increased from lower to higher rotation speeds, as shown in Fig. 6(d). The trends show an increase in output with rising rotation speeds (Su et al., 2026). Each unit measured approximately 10 V at 10 rpm, then increased to 56-64 V at 100 rpm, and finally reached a maximum V_{oc} of 107–131V at 200 rpm, with each unit capable of producing an average V_{oc} and I_{sc} of 118V and 8.8 µA.

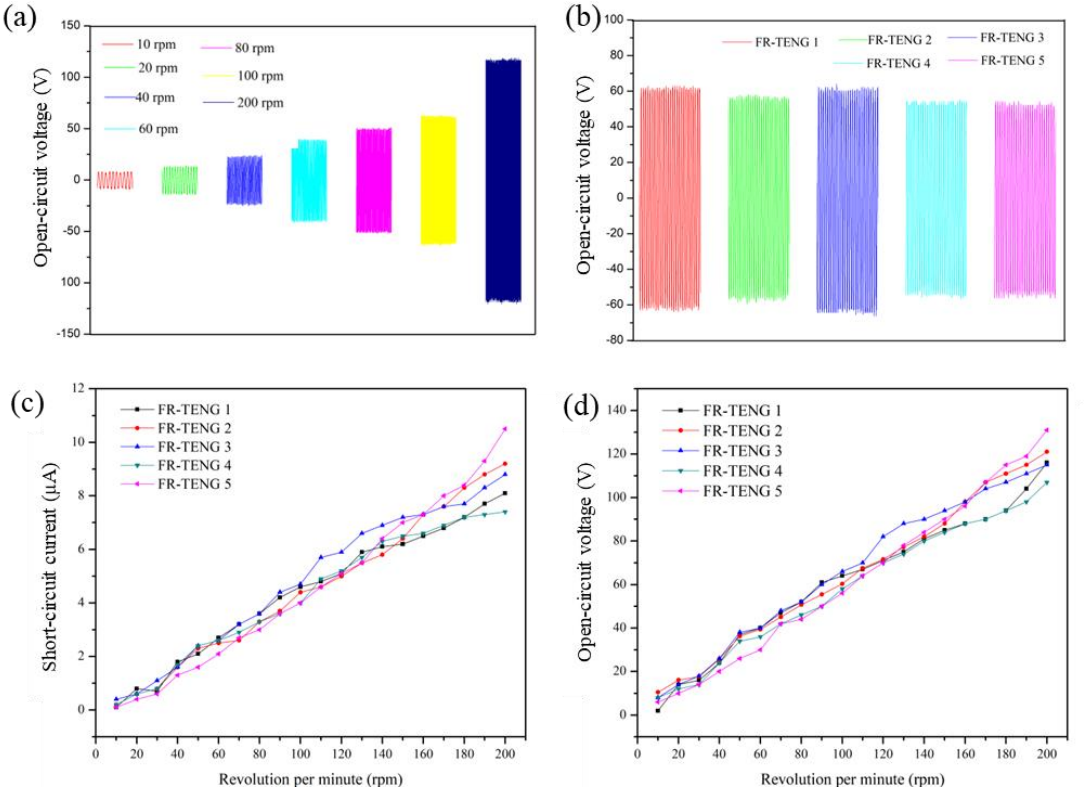

Fig. 6. The performance of the single unit FR-TENG: (a) the sinusoidal open-circuit voltage measured at different rotation speeds, (b) the measured open-circuit voltage of every single unit FR-TENG (1-5) at the rotation speed of 100 rpm, (c) the short-circuit current of every single unit at different rotation speeds and (d) the open-circuit voltage of every single unit at different rotation speeds.

FR-TENG electrical performance in a stacked arrangement

The electrical output performance *(V_{oc} and I_{sc})* of the FR-TENG in a stacked arrangement with parallel connections is comprehensively analysed in Fig. 7. The data compares the electrical performance of the stacked arrangement with that of a single FR-TENG unit at different rotational speeds. The comparison of sinusoidal V_{oc} measured for the individual unit and the stacked unit at 100 rpm is shown in Fig. 7(a). At 100 rpm, the individual unit exhibits a maximum V_{oc} of 64 V, and the stacked unit produces 137 V. The V_{oc} of the individual unit increases by 114% when five FRTENG units are connected in parallel. The V_{oc} increase is attributed to the series connection of several FR-TENG units in a stacked arrangement, which effectively amplifies the electrical output by summing the individual unit voltages in multilayer TENG designs (Firdous et al., 2021; Xia et al., 2018). In Fig. 7(b), three different rotational speeds, 10 rpm, 100 rpm, and 200 rpm, are examined for the sinusoidal waveform. The single-unit FR-TENG produces an output voltage of 6 V at 10 rpm, and the stacked arrangement produces 21 V. Confirming the proportional increase with

https://doi.org/10.24191/jmeche.v23i2.9195

increasing rotational speed, the single-unit voltage rises to 64 V at an intermediate speed of 100 rpm. At the same time, the stacked configuration reaches almost 137 V. Especially, at a high rotational speed of 200 rpm, the output voltage of the stacked FR-TENG reaches 285 V, compared to the 116 V of the individual unit, which corresponds with the theoretical expectation of voltage scaling with rotation speed due to increasing contact-separation frequency (Liu et al., 2022).

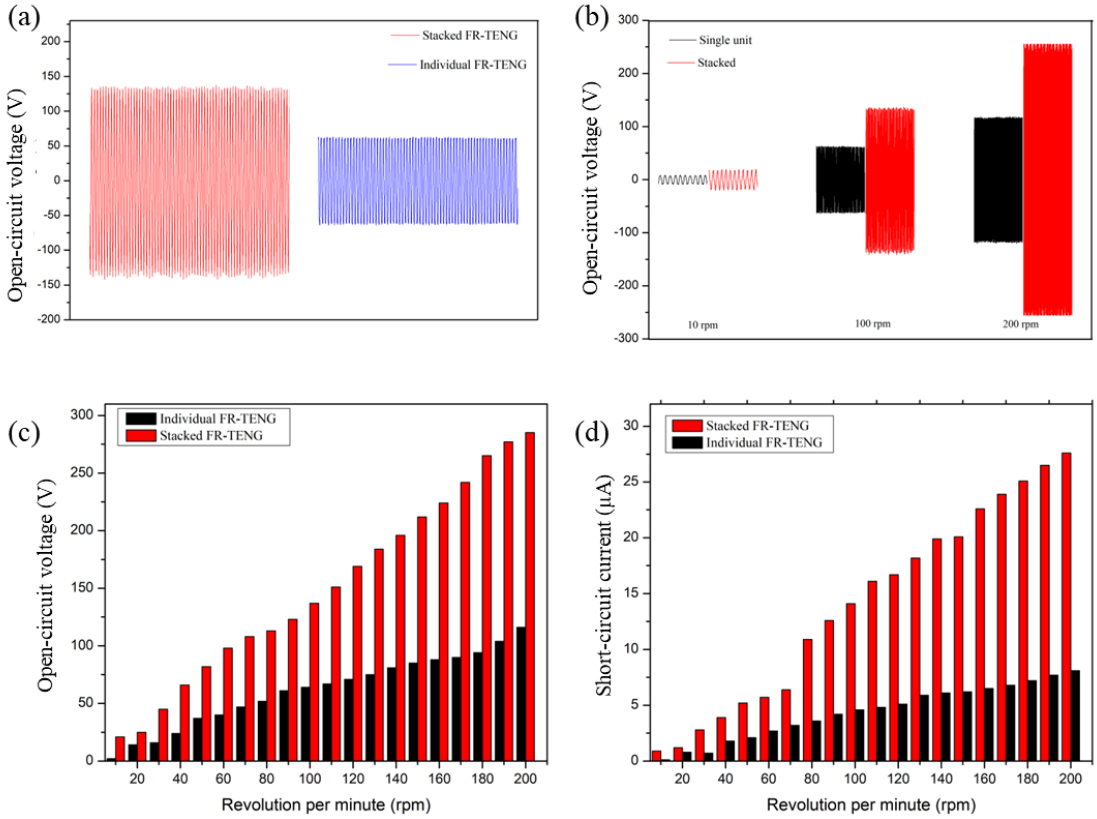

Fig. 7. The stacked arrangement of FR-TENG performance: (a) the sinusoidal voltage produced by a stacked and individual unit of FR-TENG at 100 rpm, (b) the comparison of the sinusoidal open-circuit voltage of a single unit and stacked arrangement of FR-TENG at low (10 rpm), medium (100 rpm), and high (200 rpm) rotation speeds, (c) the comparison of the open-circuit voltage between individual and stacked FR-TENG at different rpm and (d) the comparison short-circuits the current between the individual and stacked FR-TENG at different rpms.

The comparison of stacked and individual unit outputs of V_{oc} and I_{sc} is shown in Fig. 7(c) and Fig. 7(d). In Fig. 7(c), the voltage increases nearly linearly with rotation speed, a phenomenon extensively documented in performance models of frequency driven TENGs (Shao et al., 2018; Zhong et al., 2022). The individual unit shows an increase from 14 V at 20 rpm to 116 V at 200 rpm, while the stacked FR-TENG consistently produced a 145% increase in output voltage, reaching 285 V at 200 rpm. The improved performance of the stacked configuration showcases the effectiveness of multilayer integration in increasing electrical output while ensuring signal stability. A similar trend of increased output was observed in the I_{sc}, as shown in Fig. 7(d). The individual FR-TENG exhibited an I_{sc} of 0.8 μA at 20 rpm, with a proportional increase to 4.7 μA at 100 rpm, reaching a peak of about 10.5 μA at 200 rpm. The stacked FR-TENG delivers consistently superior current output, ranging from 1.2 μA at 20 rpm to 27.6 μA at 200 rpm.

https://doi.org/10.24191/jmeche.v23i2.9195

At 200 rpm, the I_{sc} increases by more than 2.4 times from the individual unit to the stacked unit. Both outputs, V_{oc} and I_{sc}, from the device increased by 145% to 240% when stacked in parallel.

The setup utilises the electrical output from stacked FR-TENGs, as illustrated in Fig. 8. Each FR-TENG was stacked and connected to the LED (light-emitting diode) board in parallel, as shown in Fig. 8(a). The actual device setup of the stacked FRTENG, as shown in Fig. 8(b), involves each unit of FRTENG being rotated simultaneously by the central rotating shaft, ensuring even rotation of the FRTENG by using the rotation speed of 100 rpm, and directly supplied to the LED boards that consists series of LEDs that arranged in parallel, the LED able to be light up by the device without the help of the rectifying circuit. The device's direct-supplied electrical capability demonstrates that the stacked configuration with a parallel arrangement can effectively simplify and increase the voltage (Yang et al., 2022). Supplying alternating current directly to the LED will reduce power losses in rectification circuits. Moreover, this demonstrates that the device can be scaled up by increasing the number of stacked layers, thereby enhancing the output for more demanding applications that require higher power consumption.

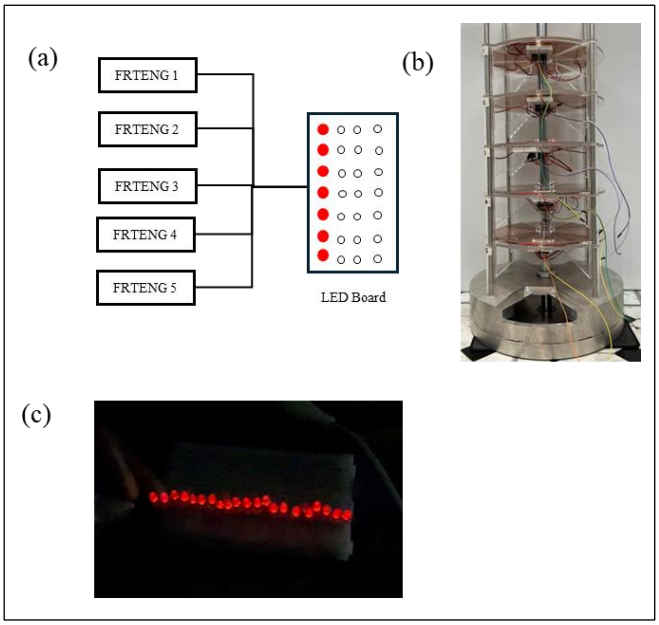

Fig. 8. Stacked unit FRTENG supplying LED: (a) the connection to the LED Boards, (b) the Stacked FR TENG setup, and (c) the LEDs light up when the Stacked FRTENG operates at 100 rpm.

CONCLUSION

This study effectively emphasizes the enhancement of a friction-based rotational triboelectric nanogenerator (FRTENG) through a stacked configuration incorporating optimized tribo-materials and surface-engineering techniques. The single-unit FR-TENG reached a peak open-circuit voltage of 131 V and a short-circuit current of 10.5 µA at 200 rpm. While the stacked configuration increased the voltage by 145% and the current by 240%, achieving 285 V and 27.6 µA, respectively. Enhancing dielectric segmentation and surface area was crucial for optimizing charge-transfer efficiency. The increased energy output effectively powered LEDs, confirming the device's suitability for small-scale energy harvesting. Moreover, supplying alternating current directly to the LEDs without rectification underscores the

https://doi.org/10.24191/jmeche.v23i2.9195

opportunity to reduce energy losses in environmental applications. The results indicate that stacked and segmented TENG designs may effectively power low-energy electronics and IoT devices. Future investigations will explore sophisticated and novel materials, power management circuits, and extensive deployment to achieve greater efficiency improvements and wider application possibilities.

ACKNOWLEDGEMENTS/ FUNDING

This research was financially supported by the Renewable Technology Program, PETRONAS Group Research & Technology (PRSB). Additionally, the authors thank the Ionic Materials and Devices (iMADE) laboratory and Universiti Teknologi MARA for providing the facilities and support.

CONFLICT OF INTEREST STATEMENT

The authors agree that this research was conducted in the absence of any self-benefit, commercial, or financial conflicts and declare that there are no conflicts of interest with the funders.

AUTHORS' CONTRIBUTIONS

The authors confirm their contribution to the paper as follows: conceptualization, methodology, and data collection: Muhammad Irsyad Missnan, Muhammad Aman Haikal Razali, Mohd Amirul Ramlan; validation, resources, and supervision: Oskar Hasdinor Hassan, Mohamad Fariz Mohamad Taib, Panu Thainiramit; analysis and interpretation of results: Muhammad Irsyad Missnan; draft manuscript preparation: Muhammad Irsyad Missnan; formal analysis: Tunku Ishak Tunku Kudin, Ahmad Sukri Ahmad, Ainnur Sherene Kamisan., Nur Hamizah Mohd Zaki All authors reviewed the results and approved the final version of the manuscript.

DATA AVAILABILITY/ SUPPLEMENTARY MATERIALS

The datasets used and/or analysed during the current study are available from the corresponding author on reasonable request

ETHICS STATEMENT

The authors declare that this research did not involve human or animal subjects. All experimental procedures were performed following the institutional Safety, Health, and Environmental (HSE) protocols of Faculty of Applied Science, Universiti Teknologi MARA (UiTM), Malaysia.

https://doi.org/10.24191/jmeche.v23i2.9195

REFERENCE

Bai, Y., Feng, H., & Li, Z. (2022). Theory and applications of high-voltage triboelectric nanogenerators. Cell Reports Physical Science, 3(11), 101108. https://doi.org/10.1016/j.xcrp.2022.101108

Chatbouri, S., Wassim, K., & Alan, J. M. (2025). High-energy efficiency of sliding triboelectric nanogenerators for mechanical energy conversion. Microsystem Technologies, 31(9), 2409-2417. https://doi.org/10.1007/s00542-025-05863-8

Chen, J., Guo, H., He, X., Liu, G., Xi, Y., Shi, H., & Hu, C. (2016). Enhancing performance of triboelectric nanogenerator by filling high dielectric nanoparticles into sponge PDMS film. ACS Applied Materials and Interfaces, 8(1), 736–744. https://doi.org/10.1021/acsami.5b09907

Fan, F. R., Tian, Z. Q., & Wang, Z. L. (2012). Flexible triboelectric generator. Nano Energy, 1(2), 328–334. https://doi.org/10.1016/j.nanoen.2012.01.004

Fang, Y., Tang, T., Li, Y., Hou, C., Wen, F., Yang, Z., Chen, T., Sun, L., Liu, H., & Lee, C. (2021). A high-performance triboelectric-electromagnetic hybrid wind energy harvester based on rotational tapered rollers aiming at outdoor IoT applications. IScience, 24(4), 102300. https://doi.org/10.1016/j.isci.2021.102300

Firdous, I., Fahim, M., & Daoud, W. A. (2021). Performance enhancement of triboelectric nanogenerator through hole and electron blocking layers-based interfacial design. Nano Energy, 82, 105694. https://doi.org/10.1016/j.nanoen.2020.105694

Gomes, A., Rodrigues, C., Pereira, A. M., & Ventura, J. (2018). Influence of thickness and contact area on the performance of PDMS-based triboelectric nanogenerators [Preprint]. arXiv. https://doi.org/10.48550/arXiv.1803.10070

Han, J. Y., Singh, H. H., Won, S., Kong, D. S., Hu, Y. C., Ko, Y. J., Lee, K. T., Wie, J. J., & Jung, J. H. (2022). Highly durable direct-current power generation in polarity-controlled and soft-triggered rotational triboelectric nanogenerator. Applied Energy, 314, 119006. https://doi.org/10.1016/j.apenergy.2022.119006

Han, M., Zhang, X., & Zhang, H. (2019). Flexible and stretchable triboelectric nanogenerator devices: toward self-powered systems. Wiley. https://doi.org/10.1002/9783527820153

Han, C. B., Du, W., Zhang, C., Tang, W., Zhang, L., & Wang, Z. L. (2014). Harvesting energy from automobile brake in contact and non-contact mode by conjunction of triboelectrication and electrostatic-induction processes. Nano Energy, 6, 59–65. https://doi.org/10.1016/j.nanoen.2014.03.009

Hao, C., Qi, B., Wang, Z., Cai, M., Cui, J., & Zheng, Y. (2023). High performance rotating triboelectric nanogenerator with coaxial rolling charge pump strategy. Micromachines, 14(12), 2160. https://doi.org/10.3390/mi14122160

He, G., Luo, Y., Zhai, Y., Wu, Y., You, J., Lu, R., Zeng, S., & Wang, Z. L. (2021). Regulating random mechanical motion using the principle of auto-winding mechanical watch for driving TENG with constant AC output – an approach for efficient usage of high entropy energy. Nano Energy, 87, 106195. https://doi.org/10.1016/j.nanoen.2021.106195

Kim, W. G., Kim, D. W., Tcho, I. W., Kim, J. K., Kim, M. S., & Choi, Y. K. (2021). Triboelectric nanogenerator: structure, mechanism, and applications. ACS Nano, 15(1), 258–287. https://doi.org/10.1021/acsnano.0c09803

https://doi.org/10.24191/jmeche.v23i2.9195

Li, Q., Liu, W., Yang, H., He, W., Long, L., Wu, M., Zhang, X., Xi, Y., Hu, C., & Wang, Z. L. (2021). Ultra-stability high-voltage triboelectric nanogenerator designed by ternary dielectric triboelectrification with partial soft-contact and non-contact mode. Nano Energy, 90(B), 106585. https://doi.org/10.1016/j.nanoen.2021.106585

Lin, L., Wang, S., Xie, Y., Jing, Q., Niu, S., Hu, Y., & Wang, Z. L. (2013). Segmentally structured disk triboelectric nanogenerator for harvesting rotational mechanical energy. Nano Letters, 13(6), 2916–2923. https://doi.org/10.1021/nl4013002

Liu, C., Liu, J., Liu, J., Zhao, C., Shan, B., Chen, N., Zhou, Z., Wang, C., Pan, X., Mi, J., & Xu, M. (2022). A wind-driven rotational direct current triboelectric nanogenerator for self-powered inactivation of seawater microorganisms. Materials Today Energy, 26, 100991. https://doi.org/10.1016/j.mtener.2022.100991

Liu, G., Xu, J., Song, X., Xu, F., Shao, B., Zhang, H., Xue, R., Song, J., Wang, X., & Wang, F. (2026). A "magic angle" TENG: integrating rotational modulation and high-performance tactile sensing via patterned nanofibers. Nano Energy, 150, 111772. https://doi.org/10.1016/j.nanoen.2026.111772

Munirathinam, K., Kim, D. S., Shanmugasundaram, A., Park, J., Jeong, Y. J., & Lee, D. W. (2022). Flowing water-based tubular triboelectric nanogenerators for sustainable green energy harvesting. Nano Energy, 102, 107675. https://doi.org/10.1016/j.nanoen.2022.107675

Naval, S., Beigh, N. T., Mukherjee, D., Jain, A., & Mallick, D. (2023). Multi-output AC/DC triboelectric generator with dual rectification. Nano Energy, 105, 108004. https://doi.org/10.1016/j.nanoen.2022.108004

Niu, S., & Wang, Z. L. (2015). Theoretical systems of triboelectric nanogenerators. Nano Energy, 14, 161–192. https://doi.org/10.1016/j.nanoen.2014.11.034

Peng, S., Feng, Y., Liu, Y., Feng, M., Wu, Z., Cheng, J., Zhang, Z., Liu, Y., Shen, R., & Wang, D. (2022). New blind navigation sensor based on triboelectrification and electrostatic induction. Nano Energy, 104(B), 107899. https://doi.org/10.1016/j.nanoen.2022.107899

Rana, S. M. S., Rahman, M. T., Zahed, M. A., Lee, S. H., Shin, Y. D., Seonu, S., Kim, D., Salauddin, M., Bhatta, T., Sharstha, K., & Park, J. Y. (2022). Zirconium metal-organic framework and hybridized Co-NPC@MXene nanocomposite-coated fabric for stretchable, humidity-resistant triboelectric nanogenerators and self-powered tactile sensors. Nano Energy, 104(A), 107931. https://doi.org/10.1016/j.nanoen.2022.107931

Ren, Z., Wu, L., Pang, Y., Zhang, W., & Yang, R. (2022). Strategies for effectively harvesting wind energy based on triboelectric nanogenerators. Nano Energy, 100, 107522. https://doi.org/10.1016/j.nanoen.2022.107522

Segkos, A., & Tsamis, C. (2023). Rotating triboelectric nanogenerators for energy harvesting and their applications. Nanoenergy Advances, 3(3), 170–219. https://doi.org/10.3390/nanoenergyadv3030010

Shao, H., Cheng, P., Chen, R., Xie, L., Sun, N., Shen, Q., Chen, X., Zhu, Q., Zhang, Y., Liu, Y., Wen, Z., & Sun, X. (2018). Triboelectric–electromagnetic hybrid generator for harvesting blue energy. Nano-Micro Letters, 10(3), 54. https://doi.org/10.1007/s40820-018-0207-3

Shao, J., Willatzen, M., & Wang, Z. L. (2020). Theoretical modeling of triboelectric nanogenerators (TENGs). Journal of Applied Physics, 128(11), 111101. https://doi.org/10.1063/5.0020961

Shrestha, K., Pradhan, G. B., Bhatta, T., Sharma, S., Lee, S., Song, H., Jeong, S., & Park, J. Y. (2023). Intermediate nanofibrous charge trapping layer-based wearable triboelectric self-powered sensor for

human activity recognition and user identification. Nano Energy, 108, 108180. https://doi.org/10.1016/j.nanoen.2023.108180

Su, J., Feng, C., Wang, Y., Guo, Y., Zhang, X., Chen, K., Li, X., & Zhang, D. (2026). Study on the response mechanism and performance of packaged TENG sensors under multimodal dynamic loads. Sensors and Actuators A: Physical, 399, 117431. https://doi.org/10.1016/J.SNA.2025.117431

Suo, G., Yu, Y., Zhang, Z., Wang, S., Zhao, P., Li, J., & Wang, X. (2016). Piezoelectric and triboelectric dual effects in mechanical-energy harvesting using BaTiO3/polydimethylsiloxane composite film. ACS Applied Materials and Interfaces, 8(50), 34335–34341. https://doi.org/10.1021/acsami.6b11108

Wang, S., Wang, Y., Liu, D., Zhang, Z., Li, W., Liu, C., Du, T., Xiao, X., Song, L., Pang, H., & Xu, M. (2021). A robust and self-powered tilt sensor based on annular liquid-solid interfacing triboelectric nanogenerator for ship attitude sensing. Sensors and Actuators A: Physical, 317, 112459. https://doi.org/10.1016/j.sna.2020.112459

Wang, W., Wu, Q., Wang, H., Chen, W., Li, W., Wu, Z., Wan, Y., Feng, Y., & Wang, D. (2024). Gas-solid two-phase flow triboelectric generator for powder triboelectrification energy collection and road early warning. Nano Energy, 120, 109170. https://doi.org/10.1016/j.nanoen.2023.109170

Wang, Z. L. (2014). Triboelectric nanogenerators as new energy technology and self-powered sensors - principles, problems and perspectives. Faraday Discussions, 176, 447–458. https://doi.org/10.1039/c4fd00159a

Wang, Z. L., Jiang, T., & Xu, L. (2017). Toward the blue energy dream by triboelectric nanogenerator networks. Nano Energy, 39, 9–23. https://doi.org/10.1016/J.NANOEN.2017.06.035

Wang, Z. L., & Song, J. (2006). Piezoelectric nanogenerators based on zinc oxide nanowire arrays. Science, 312(5771), 242–246. https://doi.org/10.1126/science.1124005

Wang, Z. L., & Wang, A. C. (2019). On the origin of contact-electrification. Materials Today, 30, 34–51. https://doi.org/10.1016/j.mattod.2019.05.016

Xia, K., Zhang, H., Zhu, Z., & Xu, Z. (2018). Folding triboelectric nanogenerator on paper based on conductive ink and teflon tape. Sensors and Actuators A: Physical, 272, 28–32. https://doi.org/10.1016/j.sna.2018.01.054

Xin, Y., Du, T., Liu, C., Hu, Z., Sun, P., & Xu, M. (2022). A ring-type triboelectric nanogenerator for rotational mechanical energy harvesting and self-powered rotational speed sensing. Micromachines, 13(4), 556. https://doi.org/10.3390/mi13040556

Xu, C., Zi, Y., Wang, A. C., Zou, H., Dai, Y., He, X., Wang, P., Wang, Y. C., Feng, P., Li, D., & Wang, Z. L. (2018). On the electron-transfer mechanism in the contact-electrification effect. Advanced Materials, 30(15), 1706790. https://doi.org/10.1002/adma.201706790

Yang, T. J., Lin, Z. H., & Lu, Y. W. (2023). Self-powered digital microfluidics driven by rotational triboelectric nanogenerator. Nano Energy, 110, 108376. https://doi.org/10.1016/j.nanoen.2023.108376

Yang, Y., Guo, W., Pradel, K. C., Zhu, G., Zhou, Y., Zhang, Y., Hu, Y., Lin, L., & Wang, Z. L. (2012). Pyroelectric nanogenerators for harvesting thermoelectric energy. Nano Letters, 12(6), 2833–2838. https://doi.org/10.1021/nl3003039

Yang, Z., Yang, Y., Liu, F., Li, B., Li, Y., Liu, X., Chen, J., Wang, C., Ji, L., Wang, Z. L., & Cheng, J. (2022). Thousandfold boosting instantaneous current of triboelectric nanogenerator based on

decoupled charge pump and discharge tube. Nano Energy, 98, 107264. https://doi.org/10.1016/j.nanoen.2022.107264

Zhang, W., Bao, W., Lü, X., & Diao, D. (2023). Friction force excitation effect on the sliding-mode triboelectric nanogenerator. Tribology International, 185, 108504. https://doi.org/10.1016/j.triboint.2023.108504

Zhao, C., Hu, G., & Yang, Y. (2022). A cantilever-type vibro-impact triboelectric energy harvester for wind energy harvesting. Mechanical Systems and Signal Processing, 177, 109185. https://doi.org/10.1016/j.ymssp.2022.109185

Zhong, Y., Yan, J., Mei, N., & Huang, C. (2022). Research on wave energy collection based on swing ship triboelectric nanogenerator. Energy Reports, 8(Supplement 12), 135–145. https://doi.org/10.1016/j.egyr.2022.10.073

Zhou, H., Liu, G., Gao, Y., Wang, Z., Qin, Y., Wang, Y., Lin, Y., Xie, Y., Chen, Y., & Zhang, C. (2021). Dual mode rotary triboelectric nanogenerator for collecting kinetic energy from bicycle brake. Advanced Energy and Sustainability Research, 2(6), 2000113. https://doi.org/10.1002/aesr.202000113

Zhou, Y., Deng, W., Xu, J., & Chen, J. (2020). Engineering materials at the nanoscale for triboelectric nanogenerators. Cell Reports Physical Science, 1(8), 100142. https://doi.org/10.1016/j.xcrp.2020.100142

Zou, H., Guo, L., Xue, H., Zhang, Y., Shen, X., Liu, X., Wang, P., He, X., Dai, G., Jiang, P., Zheng, H., Zhang, B., Xu, C., & Wang, Z. L. (2020). Quantifying and understanding the triboelectric series of inorganic non-metallic materials. Nature Communications, 11, 2093. https://doi.org/10.1038/s41467-020-15926-1

https://doi.org/10.24191/jmeche.v23i2.9195